Multiscale simulation of deployable composite structures

Yufei Long*, and Orzuri Rique Garaizar†
Purdue University, West Lafayette, IN 47907, USA

Juan M. Fernandez‡ and Andrew C. Bergan§
NASA Langley Research Center, Hampton, VA 23666, USA

Wenbin Yu¶
Purdue University, West Lafayette, IN 47907, USA

In this paper, a multiscale simulation method for analyzing deployable composite structures is presented. Effective shell properties of the composites are obtained based on Mechanics of Structure Genome (MSG) homogenization, and then implemented into a user-subroutine UGENS for structural simulation with shell elements in Abaqus. The column bending test (CBT) of a flat thin flexure and lenticular composite boom in a simplified deployer structure are studied for demonstration. A viscoelastic material model with direct integration is adopted in this paper. The CBT simulation shows good agreement with experiments during relaxation, while errors are observed when comparing residual deformation. It is shown that this CBT model can be calibrated to CBT test results. For the lenticular boom analysis, the complete process of flattening, coiling, stowage, deployment and recovery is simulated with the viscoelastic shell model.

I. Introduction

A deployable space structure occupies a small volume during launch, typically packaged to less than 1 m^3 inside a small satellite, and can be deployed in space using strain energy to stable configurations on the order of 5-20 m for small satellite missions [1]. Compared with conventional metallic deployable structures, composite deployable structures do not have joints due to the high flexibility of the constituents, achieved by using thin-ply high strain composite materials (TP-HSC) [2], which have a ply thickness of only 0.02 to 0.1 mm, and are only several plies thick. This is much thinner than conventional composites used for instance in commercial airplanes. This greatly reduces the weight of the structures. However, high flexibility also means that these kind of structures undergo large deformations during operation, and time-dependent material behavior is observed because of the long stowage time before deployment demanded usually. These factors make the analyses of deployable composite structures more challenging than traditional laminates.

*Graduate Research Assistant,School of Aeronautics and Astronautics.
†Graduate Research Assistant, School of Aeronautics and Astronautics, AIAA Student Member.
‡Research Aerospace Engineer, Structural Dynamics Branch, AIAA Member.
§Research Aerospace Engineer, Durability, Damage Tolerance, and Reliability Branch, AIAA Member.
¶Professor, School of Aeronautics and Astronautics, AIAA Associate Fellow.

In order to analyze composite deployable structures, both experimental and numerical methods have been developed. For studying the constitutive relations of TP-HSC used in deployable structures, experiments are designed to test composite flexures under large bending deformation, including the simple vertical test [3], the platen test [4, 5], the large deformation four-point bending (LD-FPB) test [6], and the column bending test (CBT) [7]. The CBT loads the specimen in compression with pinned ends offset from the specimen's neutral axis, generating a stress state close to pure bending. To have a better understanding of the distribution of stresses and strains in the specimen during the test, numerical simulations of the CBT also need to be studied. By simulating the CBT, modeling techniques, material constitutive models, and user subroutines can be verified before application to more complicated deployable boom structures. In addition, the CBT model can be used as a tool for calibrating shell properties based on the experimental data. Calibration of material properties is also possible when integrated with homogenization.

Limited work has been done in modeling and simulating the CBT experiments for TP-HSC. Rose et al. [8] used a CBT simulation in Abaqus to verify the modeling technique referred to as the coincident element method. In this method, independent layers of orthotropic elastic and isotropic viscoelastic shell elements share nodes, so that orthotropic viscoleastic behavior can be simulated with current Abaqus built-in capabilities. Gomez-Delrio and Kwok [9] analyzed the bending of a TP-HSC plate with a simplified analytical model and a finite element simulation. They found that the results from the two models match well when a uniform distribution of curvature is assumed.

Although the simulation of the CBT provides a way to study and verify the constitutive models, analysis of composite deployable structures is necessary to support practical engineering applications. Deployable composite booms undergo flattening, coiling around a hub, and stowage (relaxation) prior to launch. After launch, the booms are deployed and recover only partially the original cross-section. Due to the complexity of modeling a deployable structure with one or more booms and a coiling hub and the highly nonlinear process of coiling and deployment, many researchers have used simplified models. Both analytical [9–11] and finite element method [9, 12–15] can be found in literature. Some researchers have only focused on the flattening process [9, 12]. So far the finite element models of boom coiling, stowage, and deployment have been limited to tape spring or triangular thin-shell booms [13, 16]. Validated models capable of simulating the entire process of coiling, stowage and deploying of a deployable composite boom structure considering the time-dependent material behavior are still needed, especially for booms with complex cross-sections, such as for lenticular booms.

A multiscale simulation framework for deployable composite structures is proposed in this paper. The structural simulation at the laminate scale is the current focus. Starting from the constituent fiber and resin matrix material properties obtained from experiments, the effective linear viscoelastic stiffness matrix of shell elements can be calculated based on the mechanics of structure genome (MSG), a general method for constitutive modeling of heterogeneous materials and structures [17, 18]. SwiftComp™ [19], a finite element homogenization code based on MSG is used in this study to calculate the effective shell properties of the TP-HSC. For the structural simulation, a finite element model of the CBT is constructed in Abaqus, with the effective properties calculated from SwiftComp$^{\text{TM}}$ implemented in a user-subroutine UGENS. The validation of the shell constitutive model is implemented by comparison of simulation results to experimental data. Then, following the same procedure, the whole process of coiling, stowage and deployment of a lenticular boom is simulated. Residual deformation after deployment caused by long stowage time in both the boom longitudinal direction and cross-section is investigated. In order to use the UGENS subroutine, all the simulations in this study use the Abaqus/Standard solver.

II. MSG-Based Multiscale Simulation Framework

Due to the small thickness of TP-HSC used in deployable composite structures, the most appropriate way of simulating these structures with the finite element method is using shell elements. Based on previous studies on large bending of TP-HSC, close coupling between structural and material behavior is observed [2]. Starting from the material properties of fiber and resin matrix obtained from experiments, effective shell properties can be calculated directly based on MSG so that simplifications introduced in homogenization are minimized. Simulation of deployable composite structures following the proposed MSG-based framework includes two levels: MSG-based homogenization and structural analysis using shell element models, as shown in Fig. 1.

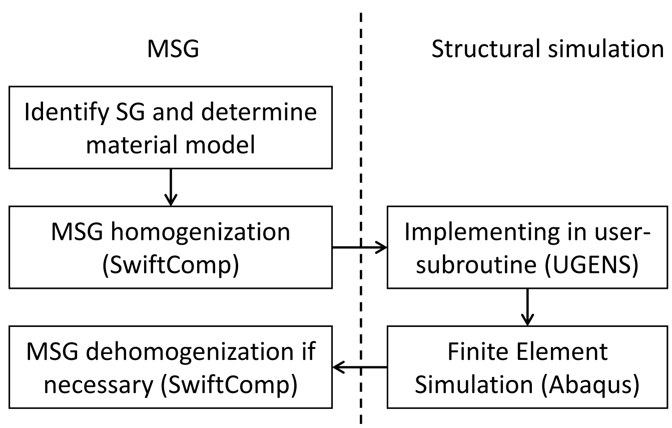

Fig. 1. Work flow of MSG-based simulation framework.

The process starts with MSG-based homogenization. First, the structure gene (SG), the smallest mathematical building block of the structure, needs to be identified. The SG includes the microscale and/or mesoscale geometry as well as the constitutive models of the materials. In this study, geometries of the SG considered are plain weave (PW), unidirectional (UD), or multidirectional laminates, depending on the application. The material model is elastic for the fiber and linear viscoelastic for the matrix. SwiftComp$^{\text{TM}}$ is used to obtain the effective shell properties by homogenization. Based on the geometry and material of the SG, input files can be prepared for homogenization using SwiftComp$^{\text{TM}}$ and effective properties can be obtained. Using the proposed framework, future work could extend the capability by adding MSG-based homogenization codes for different kinds of material constitutive models, either linear or nonlinear [20–22].

Effective properties calculated based on MSG are used in the structural simulation. For most nonlinear and some linear material models, developing a user-subroutine would be necessary. In this study, the solver for structural simulation is Abaqus/Standard, and the user-subroutine UGENS is used for implementing the effective shell properties. The effective shell properties are fitted with Prony series and then implemented in the UGENS with the direct integration method following the classical plate model, in which increments of the shell sectional forces ΔN and moments ΔM are calculated using

$$\begin{aligned} \Delta N\left(t_{n+1}\right) &= A_{eq}\Delta\epsilon\left(t_{n+1}\right) + B_{eq}\Delta\kappa\left(t_{n+1}\right) + \Omega_N \\ \Delta M\left(t_{n+1}\right) &= B_{eq}\Delta\epsilon\left(t_{n+1}\right) + D_{eq}\Delta\kappa\left(t_{n+1}\right) + \Omega_M \end{aligned} \tag{1}$$

where A_{eq}, B_{eq}, and D_{eq} are equivalent tangential stiffness matrices calculated from the Prony series of the shell properties, $\Delta\epsilon$ is the membrane strain increment, $\Delta\kappa$ is the curvature increment, Ω_N and Ω_M are column matrices determined from the loading history, t_{n+1} is the time at increment $n + 1$. Sectional forces and moments at the end of the current increment are obtained by adding the increments ΔN and ΔM to the sectional forces and moments from the previous increment. Details of the derivation of Eq. (1) can be found in [23]. In addition, it should be noted that the present formulation is a corrected version of the one presented by Zocher [24] for solid elements.

Due to the large deformation of the TP-HSC material in deployale boom applications, geometric nonlinearity is considered in the structural finite element analysis. This is consistent with MSG, as kinematic formulation of MSG is geometrically exact. Results of the structural simulation can be used for dehomogenization if the loading history follows step type behavior. The dehomogenization can show the distribution of displacement, stress and strain inside the SG at a material point.

III. CBT Simulation

In this section, the CBT structural simulation model, analysis, and results are presented. In the CBT, the rectangular flat specimen is clamped at the top and bottom edges by upper and lower fixture arms, which are pinned inside clevises. An initial angle θ exists between the fixture arms and the loading direction, creating an offset between the specimen and the loading axis. Due to this offset, when the clevises move towards each other, a moment is generated and the specimen is bent. A schematic of a CBT is shown in Fig. 2. With the initial fixture angle θ, fixture arm length l and specimen gage length s known, fixture clevis displacement δ and applied load P controlled or measured. The fixture arm angle change ϕ and moment arm r can be calculated.

The CBT specimens are constructed using M30S/PMT-F7 plain weave plies with the layup $[\pm 45]_4$. The carbon

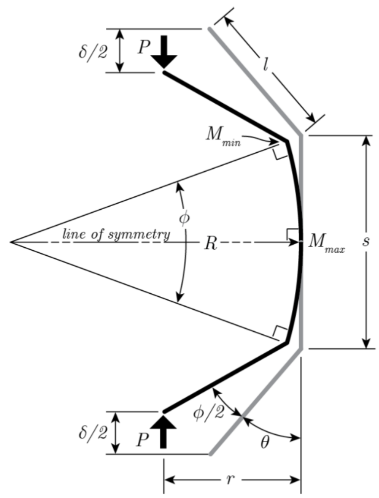

Fig. 2. Schematic of the CBT with the thick gray lines showing the initial configuration and the thick black lines showing the deformed configuration [7].

M30S fiber is treated as an elastic material and the PMT-F7 toughened epoxy resin is assumed to be linear viscoelastic. Properties of the fiber and resin are shown in Tables 1 and 2. The Prony series coefficients in Table 2 were fitted from the experimental data obtained by NASA Langley Research Center (LaRC). For woven composites, effective properties can be obtained using MSG through a two-step homogenization [25] that first calculates the effective yarn properties based on the fiber and matrix properties, and then the effective shell properties are obtained using the yarn and matrix properties.

The CBT finite element model is shown in Fig. 3. The specimen between the clamps is modeled with fully integrated four-node shell elements S4, and the clamped regions are neglected. The pins are represented by two reference points. The lower reference point (RP-1) is fixed in all degrees of freedom (DOFs) except rotation about the x-axis. The upper reference point (RP-2) allows rotation about the x-axis and displacement in the y-direction with the other DOFs held constant. Kinematic couplings are applied between the upper and lower edge of the specimen and the corresponding reference points RP-1 and RP-2, as shown in Fig. 3 by the blue lines. These couplings connect the displacement of the edges with those of the reference points rigidly, and ensure that the edges have the same rotation as the corresponding reference points to mimic the fixture arms in the experiments.

Table 1. Material properties of M30S carbon fiber [26].

E_1 (MPa)	294,000
$E_2 = E_3$ (MPa)	29,148
$G_{12} = G_{13}$ (MPa)	11,310
G_{23} (MPa)	10,000
$\nu_{12} = \nu_{13}$	0.2
ν_{23}	0.46

Table 2. Prony series coefficients of PMT-F7 resin.

s	λ_s (s)	E_s (MPa)
∞	–	1,546
1	37.0	324.7
2	1.0E+02	236.3
3	5.0E+02	7.1
4	1.0E+03	201.2
5	5.0E+03	81.5
6	1.0E+04	89.5
7	5.0E+04	223.9
8	1.0E+05	19.5
9	5.0E+05	109.3
10	1.0E+06	60.0
11	5.0E+06	0.8

The analysis consists of four steps, as follows referred to as folding, relaxation, unfolding, and recovery. The CBT is a quasi-static process so all of the steps are implemented as general static steps in Abaqus. In the folding step, end shortening, implemented through a y-displacement boundary condition, is applied to RP-1 such that the specimen bends. Then, this configuration is kept constant for a specified period of time to allow stress relaxation. After relaxation, the displacement boundary condition in the y-direction at RP-1 is removed, so that the reaction forces at the reference points become zero and the specimen is unfolded by its internal stress. The unfolded configuration is also kept for some time, during which the specimen gradually recovers its original shape. Geometric nonlinearity is enabled in all the steps.

The specimen and test parameters of the CBT model shown in Table 3 are used in order to compare with existing experimental data [27]. The displacement in the folding step is applied at a rate of 12.7 mm/min, resulting in a load time of 2 min, and the times for relaxation and recovery are 6 h and 2 h respectively.

Table 3. Specimen and test parameters of the CBT model.

CBT fixture arm length l (mm)	25.4
Specimen width d (mm)	25.4
Specimen gage length s (mm)	27.432
Fixture arm initial angle θ (rad)	0.0712
Fixture total displacement δ (mm)	25.4
Specimen thickness h (mm)	0.276

In experiments, it is observed that the CBT generates a nonuniform distribution of curvature in the specimen. This feature is successfully captured by the simulation. Defining x_i as the local coordinates of the TP-HSC specimen, as shown in Fig. 3. The local coordinates move along with the specimen during deformation. Simulation result of the curvature κ_{11} along the red line in Fig. 3 is shown in Fig. 4, with the distance normalized by the specimen gage length.

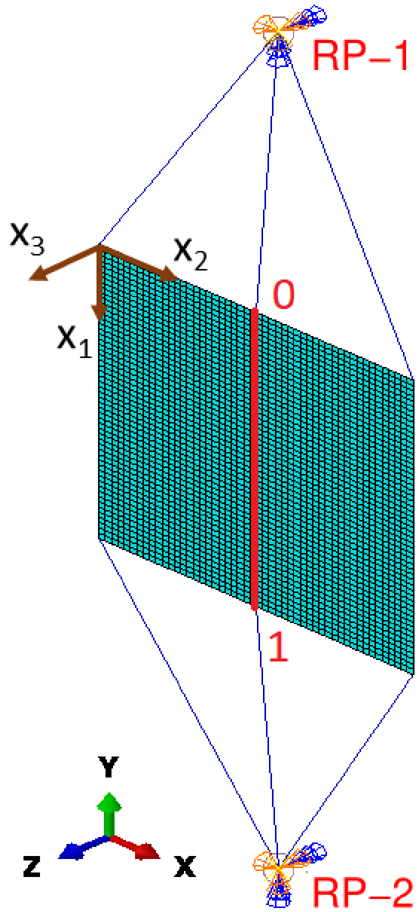

Fig. 3. CBT model in Abaqus/CAE.

The curvature κ_{11} at the center is 0.071 mm^{-1}, which is 34% larger than the value of 0.053 mm^{-1} at the upper and lower edges. However, data reduction procedure used to generate the experimental results idealizes the curvature to be constant in the specimen, so an analogous data reduction for the simulation is required for direct comparison. The curvature is computed using the total fixture arm rotation angle change ϕ and specimen gage length s with the formula [7]

$$\kappa = \frac{\phi}{s} \tag{2}$$

where the total fixture arm rotation angle change is obtained from the rotation of the reference point ϕ_{rp}, and calculated by Abaqus as $\phi = 2\phi_{rp}$.

The simulation results reveal that not only the curvature κ_{11}, but also the section moments M_{11} and M_{22} have non-uniform distribution, as shown in Fig. 5. Different from the curvature κ_{11}, the moments not only vary in the gage length direction, but also in the width direction. For comparison with experiments, a maximum moment M_{max} is

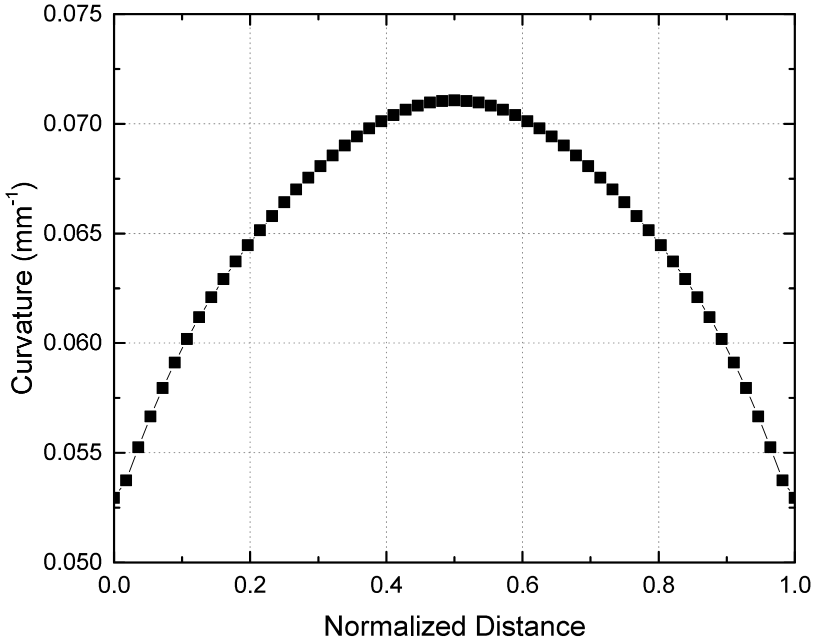

Fig. 4. Curvature κ_{11} along the vertical center line.

calculated with the applied load P and maximum moment arm r [7]

$$M_{max} = Pr \tag{3}$$

where the load P equals to the vertical reaction force output at the reference point of Abaqus, and moment arm r can be calculated with

$$r = u_3 + r_0 \tag{4}$$

where u_3 is the normal displacement at the center of the specimen obtained from Abaqus and r_0 is the initial offset.

The curvature history during the folding step is shown in Fig. 6. It can be seen that the simulation and experiments follow the same trend and their magnitude is close. Subsequently, during the relaxation step, stress in the specimen is decreasing with time because of viscoelasticity, resulting in strain energy dissipation. During the relaxation time of 6 h, the predicted strain energy dissipation is 2%. An effective bending stiffness D_{11}^* is calculated and used for comparison with experiments

$$D_{11}^* = \frac{M_{max}/d}{\kappa} \tag{5}$$

History of D_{11}^* during relaxation are plotted in Fig. 7. It can be observed that the simulation has a small underprediction

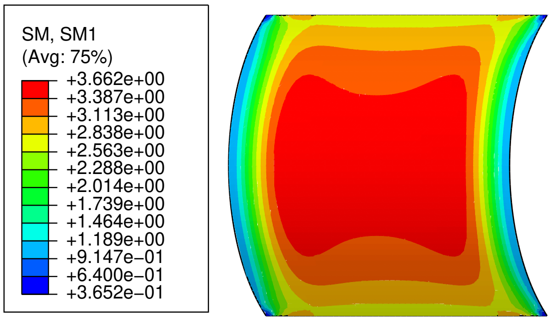

(a) Contour plot of section moment M_{11} at the start of relaxation.

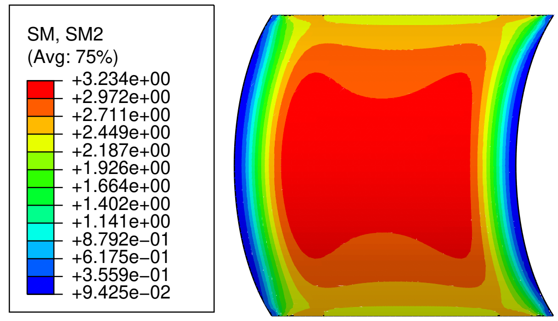

(b) Contour plot of section moment M_{22} at the start of relaxation.

Fig. 5. Non-uniform distribution of section moments in the specimen.

but comparing to the difference between the two experimental results, simulation result is very accurate. The underprediction is likely to be caused by the small overprediction of the curvature that can be seen in Fig. 6.

In order to evaluate the capability of the present method of predicting the residual deformation, the predicted and measured curvatures are compared in the unfolding and recovery stages, as shown in Fig. 8. The comparison of residual deformation after relaxation shows disagreement, especially in the final steady-state curvature. The curvature values during relaxation, after unfolding and after recovery are shown in Table 4. The curvature in the "After unfolding" column of Table 4 is approximate because in the experimental data there is no way to identify the separation between the unfolding and relaxation steps while in simulation they have to be in separate steps and the time for each steps clearly defined. The experimental values after unfolding were selected based on the curvature change being much smaller than previous data points, but this does not necessarily mean that reaction force at the loading head is zero, the way the unfolding step gets defined in the simulation. However, this difference has a small influence on the residual curvature during recovery as long as the step time of unfolding is short compared with the recovery time. Based on the above analysis and observing the curve in Fig. 8, another possible cause for the disagreement in residual curvature is viscoplasticity, as the disparity between the computed and experimental results is relatively constant through the recovery period. The large surface strains imposed on the specimens during the CBT likely caused some degree of plastic deformation. To understand the effect of viscoplasticity, future work should consider a viscoplastic material model and a nonlinear shell model.

The presented simulation framework also has the potential to be used for calibration. To demonstrate this capability, a calibration of the shell bending stiffness in the axial x_1-direction D_{11} is carried out. This calibration does not involve MSG homogenization, but it can be easily integrated into the algorithm in future work to calibrate resin material properties. Initial values of the Prony series coefficients of D_{11} and the values after calibration are shown in Table 5.

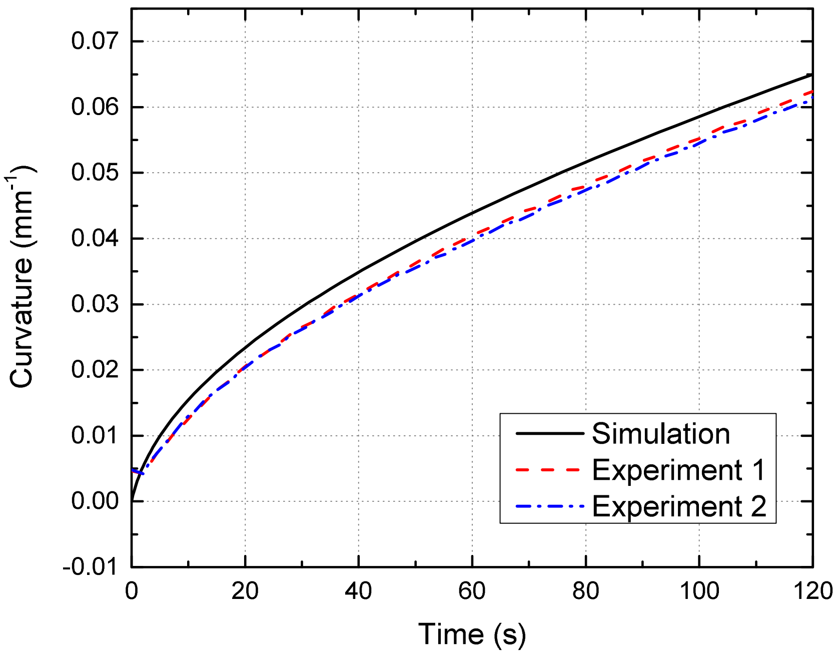

Fig. 6. Curvature history during folding.

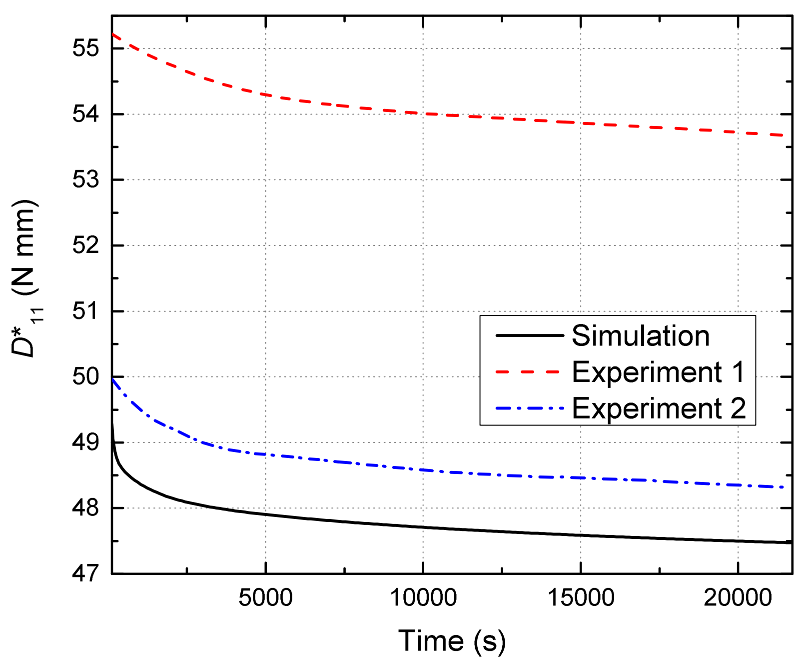

Fig. 7. History of effective bending stiffness D^*_{11} during relaxation.

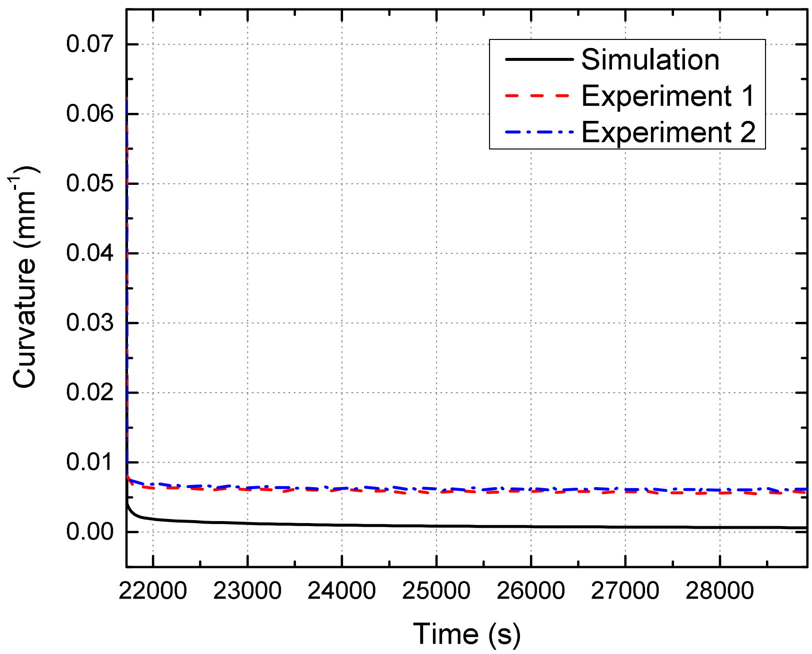

Fig. 8. Residual curvature after relaxation.

Table 4. Residual curvature after relaxation (mm^{-1}).

Curvature	Relaxation	After unfolding (Approx.)	After recovery
Simulation	0.06500	0.004130	0.0006444
Experiment 1	0.06239	0.007749	0.005936
Experiment 2	0.06153	0.008352	0.006154

Table 5. Prony series coefficients of D_{11} before and after calibration.

s	λ_s	$D_{11,s}$ (N·mm)	
		Initial	After calibration
∞	–	47.927600	45.246725
1	10	0.076000	0.000000
2	10^2	0.513000	0.348000
3	10^3	0.434500	0.403250
4	10^4	0.217800	0.434050
5	10^5	0.487300	1.629175
6	10^8	1.000000	2.595000

In this study, only D_{11} is calibrated, and other terms in the D matrix are held constant. The A matrix is estimated based on the relation

$$A_{ij} = D_{ij}\frac{12}{h^2} \tag{6}$$

where h is the thickness of the specimen. The parameters to be calibrated are $D_{11,m}$ with $m = 1$ to 6, indicating the six terms in the Prony series. The summation of all terms is kept constant during calibration, so that $D_{11,\infty}$ can be calculated. The calibration is conducted using the Dakota optimization software [28] as follows. At the beginning of the calibration, an initial value for D_{11} is written into a UGENS by Dakota, and this UGENS is used for a CBT simulation in Abaqus. After that, a post-processing script computes the effective bending stiffness D^*_{11}, which is a time-dependent curve and it can be directly compared with the curve calculated with experimental results. An error is evaluated using error sum of squares (SSE)

$$SSE = \sum\left(D^*_{11,simulation} - D^*_{11,experiment}\right)^2 \tag{7}$$

and the SSE is passed to Dakota, based on which a new set of $D_{11,m}$ is generated and the UGENS is updated. This iteration process is repeated until the SSE is converged to a minimum or the number of iterations reaches a preset value.

In this case study, calibration is judged converged by Dakota after 423 iterations, with the best results obtained at iteration 408. SSE history is shown in Fig. 9. The initial SSE is 18.7817, and after calibration, SSE is minimized to

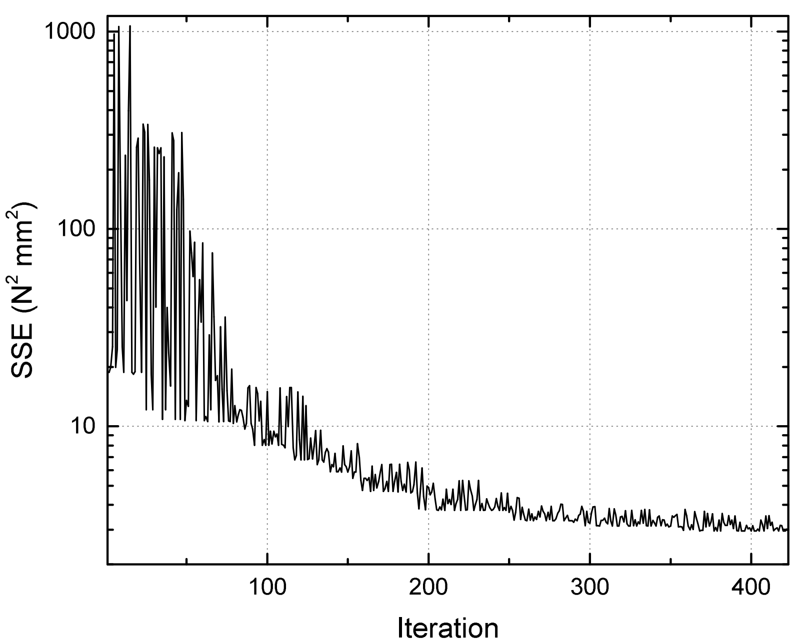

Fig. 9. SSE history.

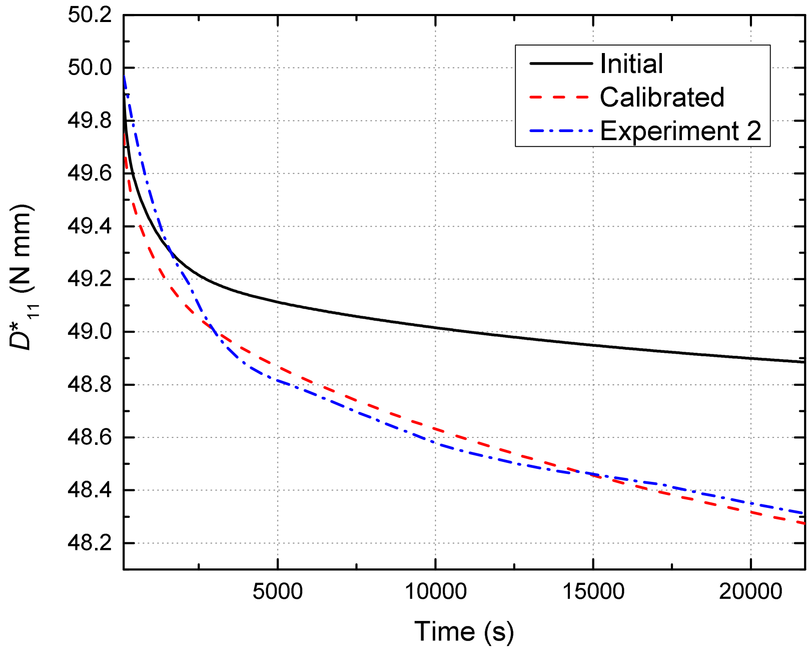

Fig. 10. History of effective bending stiffness D^*_{11} during the relaxation step before and after calibration.

be 2.9520. It can be seen that after the trials before iteration 100 that leads to very large error, SSE remains low and finally converged after about 300 iterations. The D^*_{11} during relaxation is shown in Fig. 10 for the initial material model calculated by SwiftComp, the calibrated material model, and one of the experiments. It can be observed that compared with the properties directly computed using SwiftComp^{TM}, using the calibrated data makes D^*_{11} have a faster relaxation, agreeing better with the experiment.

IV. Deployable Lenticular Boom and Hub Simulation

To understand the behavior of TP-HSC in deployable boom structures, both the boom and coiling hub need to be simulated to study the effect of coiling, stowage, and deployment. The boom is coiled to the hub by wrapping around it. This coiled configuration is kept during stowage, which can be as long as several years. For deployment, the hub is rotated in the opposite direction and the boom unwraps to its natural extended form. Differences in the boom's cross section after deployment and recovery due to the viscoelastic-viscoplastic nature of the constituent TP-HSC materials can have a large impact on the structural performance of the boom. For simulating this process, the boom is modeled using shell elements and the hub by a rigid cylindrical surface. Compared to the high flexibility of the boom, the hub has a much larger stiffness, so it can be modeled as a rigid body.

In this study, the boom has a lenticular cross-section, which consist of two Ω-shaped shells bonded together along

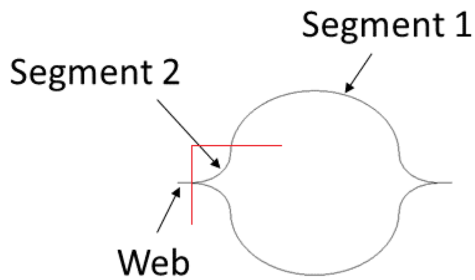

Fig. 11. Lenticular boom cross-section showing the various shell segments.

Table 6. Cross-sectional geometric parameters of the lenticular boom.

Segment 1 Radius (mm)	Segment 2 Radius (mm)	Subtended Angle (°)	Flattened Height (mm)	Web Width (mm)
26.5	12	90	130	4.5

flat regions called the webs. Geometric parameters of the cross-section are listed in Table 6, with the definition of the various shell segments based on [29], as shown in Fig. 11. Notice the subtended angle for segment 1 and 2 has to be the same because of continuity. The layup in segment 1 consists of a unidirectional axial ply between two off-axis plain weave plies, $[45_{PW}/0_{UD}/45_{PW}]$. In segment 2 and the web, the layer of plain weave composite on the inner side of the boom is dropped. In the web, a layer of epoxy film is added for joining the two shells together. Both the epoxy film and plain weave composites are considered viscoelastic materials. In the finite element model, these three sections have different effective properties due to different layups and materials. The length of the boom is 880 mm and the radius of the hub is 90 mm.

Due to the complexity of the problem, some simplifications have been adopted to avoid convergence issues. The finite element model of the deployable boom structure is shown in Fig. 12. In addition to the boom and the hub, two

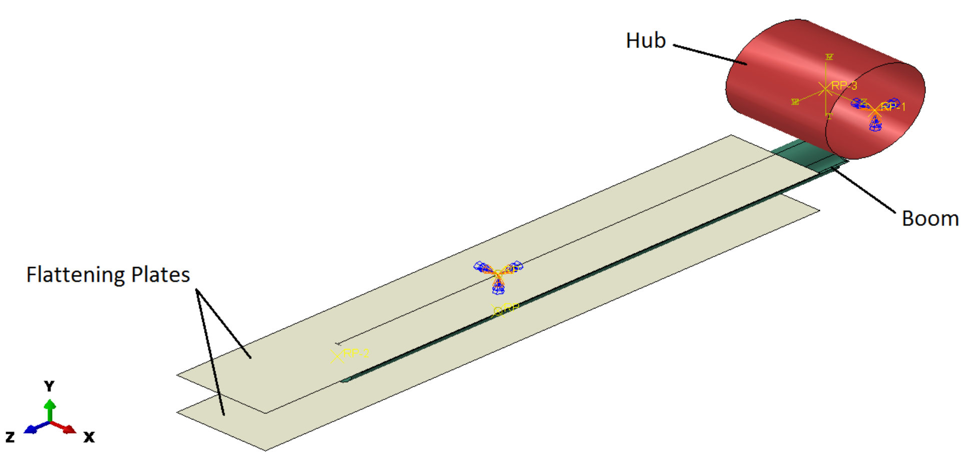

Fig. 12. Model of the deployable boom structure in Abaqus CAE.

rigid plates are also included in the model to aid in the boom coiling and deployment process. Different from reality, the whole boom is flattened all together by moving the rigid plates towards each other, so that convergence limitations caused by local buckling during the transition from the lenticular cross-section to the flattened cross-section in the boom segment near the hub can be avoided. This modeling technique can be justified as coiling and deployment are finished in a short time compared to the stowage time. The way this simplified flattening process occurs has little impact on the total energy dissipation, which is the main source of residual deformation. To also ensure convergence, an implicit dynamic quasi-static step is used in Abaqus/Standard for flattening, coiling and deploying steps, while a general static step is used for stowage step for better accuracy. A kinematic coupling between a reference point located at the center of the hub and the nodes at the hub-end of the boom is applied as the driver for coiling and deployment. After the boom is flattened, rotation is only applied to the reference point at the center of the hub while the hub itself remains fixed, acting as a rigid support for the boom to slide on during the coiling process. This technique avoids applying multiple contacts to fix the boom on the hub, and thus reducing complexity of the model. A tension force of 104 N in the z-direction is applied on the free end of the boom at the start of coiling and kept until the deployment is finished. The flattening plates are also kept in place until deployment is finished.. These features greatly help stabilize the model during deployment so that convergence can be improved. During coiling and deployment, the hub is rotated with an angular velocity of 40 rad/s (382 rpm), which is much higher than the speed of 1 rpm in the real application. Counterintuitively, it is observed that using a high rotational speed stabilizes the structures more, which allows a larger increment size that reduces the computational cost, and makes convergence issues occur less frequently. This may be caused by the way Abaqus/Standard handles the numerical damping in a quasi-static analysis. The adoption of a fast rotational speed can also be justified by the relatively short time of coiling and deployment compared with the stowage and recovery times. For obtaining numerical results, a stowage time of 30 days was used, and a recovery free-standing period of 24 h was considered after deployment. This model is referred to as the baseline model, as an improved version of the model is introduced below.

Contour plots of the residual curvature in both directions after the 24 h recovery are shown in Fig. 13. There is no obvious residual curvature in the longitudinal direction ($SK1$), while residual curvature with different signs in segment 1 and 2 can be observed in the hoop direction ($SK2$). A plot of $SK1$ along the symmetry line of the inner shell (shell closest to the hub) is shown in Fig. 14 and referred to as the baseline model. Likewise, a plot of $SK2$ along the Ω-shaped hoop line at the midspan of the inner shell is shown in Fig. 15.

From Fig. 14 it can be seen that residual curvature in the longitudinal direction only exists at the boom free ends, which is caused by the boundary effects. Considering the short length of the boom, and also its high structural stiffness if treated as a beam, it is reasonable to have negligible values outside the boundary regions. On the other hand, residual curvature in the hoop direction is much more pronounced. The opposite curvature signs of segments 1 and 2 are caused by their initial curvature. After 24 h of recovery, the maximum residual curvature was reduced by 88.3%.

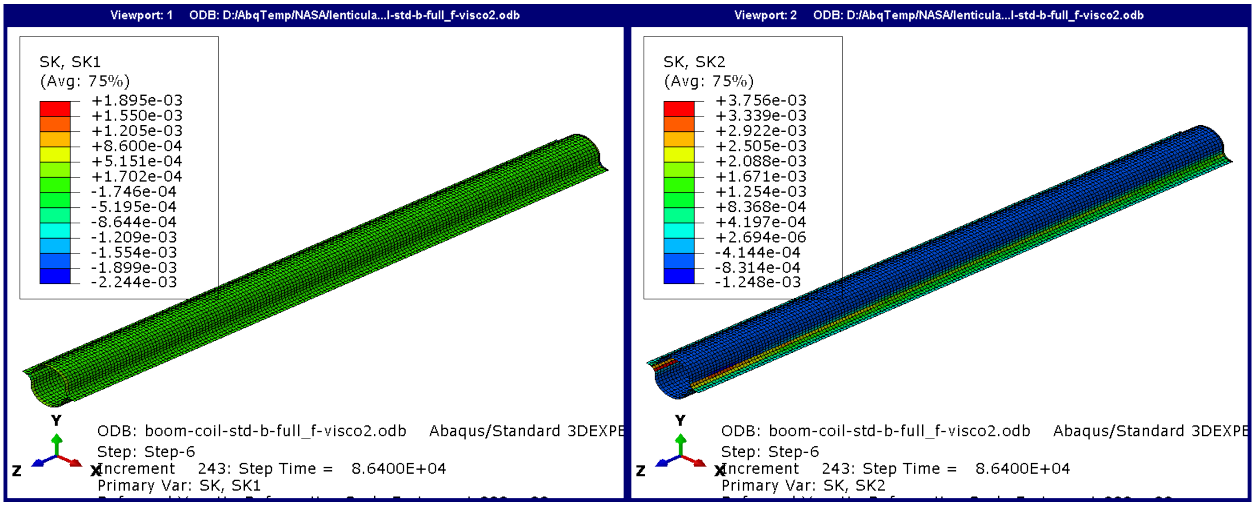

Fig. 13. Contour plots of the residual curvature after recovery.

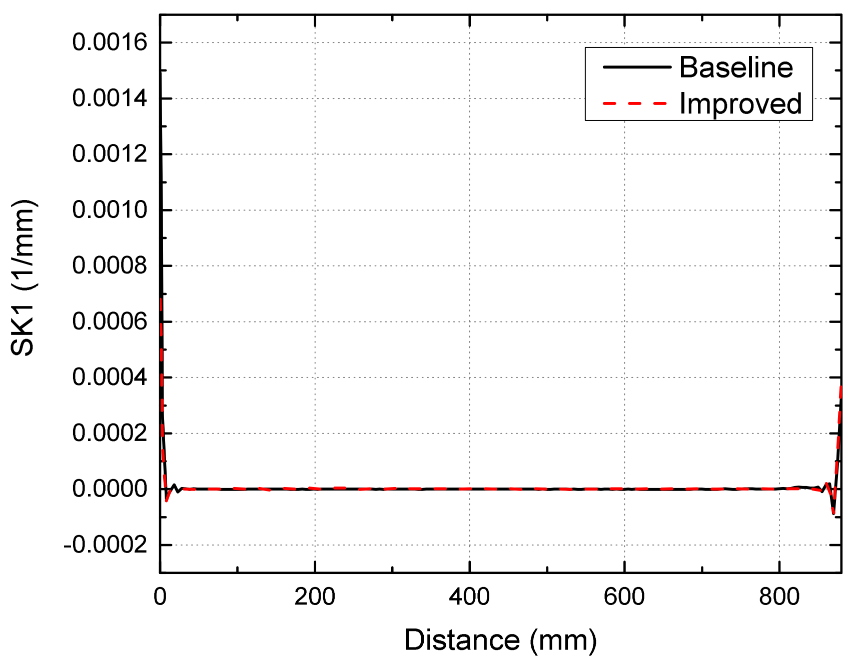

Fig. 14. Residual curvature in the longitudinal direction along the symmetry line of the inner shell.

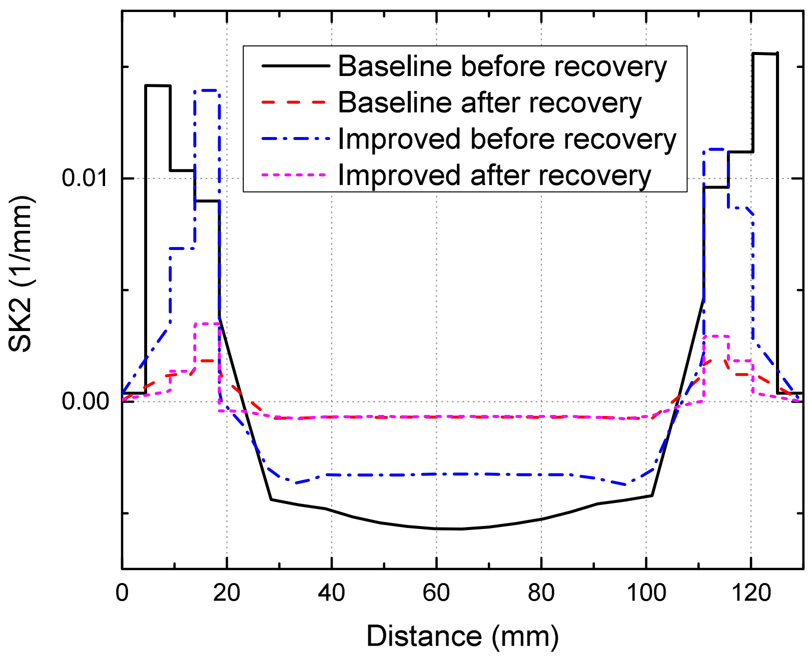

Fig. 15. Residual curvature in hoop direction vs. hoop position at the midspan of the for the inner shell.

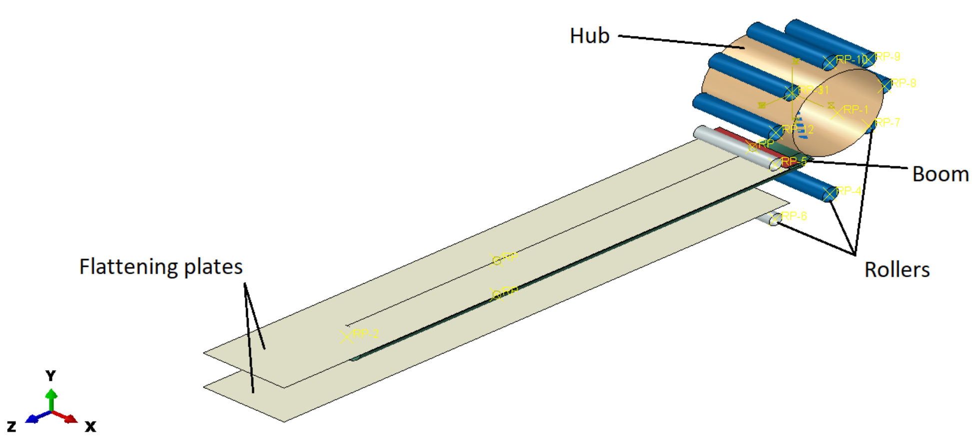

Fig. 16. Improved model of the deployable boom structure in Abaqus/CAE.

Table 7. Forces applied to the radial hub rollers.

Roller	1	2	3	4	5	6	7
Force (N)	20	21	11	11	6	6	21

In the simplified baseline model, the tension force and flattening plates are present during the stowage and deployment process. Although this is partly justified by the step times, this setup is far from reality. It should still be noticed that (1) the existence of an axial tension force and flattening plates may affect the structural behavior during deployment, and (2) the effect of an axial tension force during stowage may not be negligible. Consequently, the baseline model was improved to remove the tension force and flattening plates after coiling. The improved model has cylindrical rollers to hold the boom in the stowed configuration, as shown in Fig. 16. There are two kinds of rollers in the model, 7 surrounding the hub radially (blue in Fig. 16) and a pair below and above the boom, called nip rollers (gray in Fig. 16). Forces applied on each roller are shown in Table 7, with the magnitudes artificially increased from the design values to numerically improve stability.

In addition, all radial rollers have linear springs with a stiffness of 1 N/mm to provided larger compressive force if the boom tends to pop out from the hub during deployment. The nip rollers serve the purpose of controlling the deployment direction, which was initially done by the flattening plates in the baseline model. The nip rollers are fixed 13 mm apart for controlling the direction and preventing the boom from oscillating during deployment.

With the same stowage and recovery time as the baseline model, similar residual curvature distributions in the longitudinal and hoop directions are observed. The plot of curvature $SK1$ along the symmetry line of the inner shell is shown in Fig. 14 and referred to as the improved model. Likewise, the plot of curvature $SK2$ along the hoop line at the midspan of the inner shell is shown in Fig. 15. The residual curvature in the longitudinal direction is still negligible, while there is still significant deformation in the hoop direction. The 24 h recovery step reduces the residual curvature to 25% of the original value. The complexity of the boom coiling simulation around a hub makes a quantitative comparison between the two models challenging. One reason for the differences between the two models in Fig. 15 is caused by the rollers, as the boom tends to pop out from the hub during deployment, which is an interesting dynamic phenomenon that requires further investigation.

V. Conclusion

This paper presented a multiscale simulation framework for deployable composite structures. With micro and mesoscale homogenization using mechanics of structure genome (MSG), the unique geometric (e.g., spread-tow woven fabric) and material (e.g., viscoelastic resin) intricacies of thin-ply high strain composites (TP-HSC) can be represented in shell section properties. A CBT and a lenticular boom coiling/deploying around a hub are studied using the proposed simulation framework. Linear viscoelastic material properties are considered, and the effective shell properties are fitted with Prony series coefficients and then implemented as a user-subroutine using UGENS in Abaqus.

In the finite element simulation of the CBT, nonuniform distributions of deformation and stress are observed over the specimen. Comparison with experimental results of the curvature during folding, and bending stiffness during relaxation, and residual curvature immediately after unfolding show good qualitative agreement. However, there are deviations in the particular values obtained from simulation and experiments. The average curvature levels during specimen folding were overpredicted by the model, though the bending stiffness D^*_{11} matched well. The laminate bending stiffness relaxation was underpredicted by the simulation over the 6 h process. The residual curvature computed immediately after specimen unfolding was underpredicted by the model by a factor of two with respect to the experimental data. After recovery at zero load, this residual curvature discrepancy increased, with the model overpredicting recovery by an order of magnitude compared to the experimental results. Possible reasons for the deviations include the inaccuracies introduced by the experimental devices, and viscoplasticity, which is not included in the current material model. A calibration of the specimen bending stiffness D_{11} using Dakota is also presented for demonstration purposes. The SSE of the effective bending stiffness D^*_{11} is reduced by 84%.

In the simulation of the TP-HSC boom and the hub, the boom is modeled using shell elements and the hub using rigid elements. As the lenticular boom has a complex cross-section geometry and the simulation involves multiple contact behavior, several simplifications were introduced to avoid convergence difficulties. Numerical studies were carried out with two models. Results from both models show residual curvature is negligible in the longitudinal direction, but significant in the hoop direction. A 24-h recovery greatly reduces residual deformation after deployment by more than 70%. The phenomenon of the boom popping out from the hub during deployment is only captured by the improved model.

While the proposed framework is demonstrated to be an effective way of multiscale simulation for common TP-HSC structures, further work is still needed to increase accuracy in the predictive model. This includes the introduction of nonlinear material behaviors, such as viscoplasticity or damage, and additional validation studies at the coupon and component level scales.

Funding Sources and Acknowledgments

This research was partially supported by the NASA Small Business Technology Transfer (STTR) program's Phase I project T12.01-3920 with contract number 80NSSC19C0530. Also by the Space Act Agreement SAA-29213, Annex 2, between Purdue University and NASA LaRC. The views and conclusions obtained herein are those of the authors and should not be interpreted as necessarily representing the official policies or endorsement, either expressed or implied of the funding agency.

References

[1] Fernandez, J., "Advanced Deployable Shell-Based Composite Booms For Small Satellite Structural Applications Including Solar Sails," *4th International Symposium on Solar Sailing, Kyoto*, 2017.

[2] Murphey, T. W., Francis, W., Davis, B., Mejia-Ariza, J., Santer, M., Footdale, J. N., Schmit, K., Soykasap, O., Guidanean, K., and Warren, P. A., "High Strain Composites," *2nd AIAA Spacecraft Structures Conference*, 2015, p. 0942.

[3] Yee, J., and Pellegrino, S., "Folding of Woven Composite Structures," *Composites Part A: Applied Science and Manufacturing*, Vol. 36, No. 2, 2005, pp. 273–278.

[4] Yee, J., and Pellegrino, S., "Biaxial Bending Failure Locus for Woven-Thin-Ply Carbon Fibre Reinforced Plastic Structures," *46th AIAA/ASME/ASCE/AHS/ASC Structures, Structural Dynamics and Materials Conference*, 2005, p. 1811.

[5] Yee, J., and Pellegrino, S., "Composite Tube Hinges," *Journal of Aerospace Engineering*, Vol. 18, No. 4, 2005, pp. 224–231.

[6] Sanford, G. E., Ardelean, E. V., Murphey, T. W., and Grigoriev, M. M., "High Strain Test Method for Thin Composite Laminates," *16th International Conference on Composite Structures. Porto, Portugal*, 2011.

[7] Fernandez, J. M., and Murphey, T. W., "A Simple Test Method for Large Deformation Bending of Thin High Strain Composite Flexures," *2018 AIAA Spacecraft Structures Conference*, 2018, p. 0942.

[8] Rose, T., Calish, J., and Lopez Jimenez, F., "Modeling of Viscoelasticity in Thin Flexible Composites using Coincident Element Method," *AIAA Scitech 2020 Forum*, 2020, p. 0693.

[9] Gomez-Delrio, A., and Kwok, K., "Stowage and Recovery of Thin-ply Composite Deployable Structures," *AIAA Scitech 2020 Forum*, 2020, p. 0205.

[10] Bai, J., Xiong, J., Gao, J., and Yi, X., "Analytical Solutions for Predicting In-Plane Strain and Interlaminar Shear Stress of Ultra-Thin-Walled Lenticular collapsible composite tube in fold deformation," *Composite Structures*, Vol. 97, 2013, pp. 64–75.

[11] Brinkmeyer, A., Pellegrino, S., and Weaver, P. M., "Effects of Long-Term Stowage on the Deployment of Bistable Tape Springs," *Journal of Applied Mechanics*, Vol. 83, No. 1, 2016, p. 011008.

[12] Hu, Y., Chen, W., Gao, J., Hu, J., Fang, G., and Peng, F., "A Study of Flattening Process of Deployable Composite Thin-Walled Lenticular Tubes under Compression and Tension," *Composite Structures*, Vol. 168, 2017, pp. 164–177.

[13] Cox, K., and Medina, K. A., "Scalability of Triangular Rollable and Collapsible Booms," *AIAA Scitech 2019 Forum*, 2019, p. 2026.

[14] Yang, H., Liu, L., Guo, H., Lu, F., and Liu, Y., "Wrapping Dynamic Analysis and Optimization of Deployable Composite Triangular Rollable and Collapsible Booms," *Structural and Multidisciplinary Optimization*, Vol. 59, No. 4, 2019, pp. 1371–1383.

[15] Leclerc, C., and Pellegrino, S., “Reducing Stress Concentration in the Transition Region of Coilable Ultra-Thin-Shell Booms,” *AIAA Scitech 2019 Forum*, 2019, p. 1522.

[16] Scherbarth, M., and Taha, M. R., “Stowage Testing and Modeling of Viscoelastic Composite Tape Springs,” *AIAA Scitech 2019 Forum*, 2019, p. 1748.

[17] Yu, W., “A Unified Theory for Constitutive Modeling of Composites,” *Journal of Mechanics of Materials and Structures*, Vol. 11, No. 4, 2016, pp. 379–411.

[18] Yu, W., “Simplified Formulation of Mechanics of Structure Genome,” *AIAA Journal*, 2019, pp. 1–9.

[19] Yu, W., “SwiftComp$^{\text{TM}}$ User Manual - Version 2.1,” , 2020. URL `https://cdmhub.org/resources/scstandard/supportingdocs`.

[20] Jiang, F., and Yu, W., “Nonlinear Variational Asymptotic Sectional Analysis of Hyperelastic Beams,” *AIAA Journal*, Vol. 54, No. 2, 2016, pp. 679–690.

[21] Jiang, F., and Yu, W., “Damage Analysis by Physically Nonlinear Composite Beam Theory,” *Composite Structures*, Vol. 182, 2017, pp. 652–665.

[22] Zhang, L., and Yu, W., “Variational Asymptotic Homogenization of Elastoplastic Composites,” *Composite Structures*, Vol. 133, 2015, pp. 947–958.

[23] Long, Y., Rique Garaizar, O., Yu, W., Fernandez, J. M., and Bergan, A. C., “Simulation of Column Bending Test Based on Mechanics of Structure Genome,” *Under review*, 2020.

[24] Zocher, M. A., Groves, S. E., and Allen, D. H., “A three dimensional finite element formulation for thermoviscoelastic orthotropic media,” *International Journal for Numerical Methods in Engineering*, Vol. 40, No. 12, 1997, pp. 2267–2288.

[25] Liu, X., Tang, T., Yu, W., and Pipes, R. B., “Multiscale Modeling of Viscoelastic Behaviors of Textile Composites,” *International Journal of Engineering Science*, Vol. 130, 2018, pp. 175–186.

[26] Yapa Hamillage, M., Kwok, K., and Fernandez, J. M., “Micromechanical Modeling of High-Strain Thin-Ply Composites,” *AIAA Scitech 2019 Forum*, 2019, p. 1751.

[27] Fernandez, J. M., Salazar, J., Hamillage, M. Y., Gomez-Delrio, A., and Kwok, K., “Large Deformation Bending Relaxation of Thin Ply Composites Laminates,” *22nd International Conference on Composite Materials*, 2019.

[28] *Dakota, A Multilevel Parallel Object-Oriented Framework for Design Optimization, Parameter Estimation, Uncertainty Quantification, and Sensitivity Analysis: Version 6.11 User’s Manual*, Sandia National Laboratories, 2019.

[29] Lee, A. J., and Fernandez, J. M., “Inducing Bistability in Collapsible Tubular Mast Booms with Thin-Ply Composite Shells,” *Composite Structures*, 2019, p. 111166.